Microwave bone imaging: a preliminary scanning system for proof-of-concept

Giuseppe Ruvio[1] ✉, *Antonio Cuccaro*[2], *Raffaele Solimene*[2], *Adriana Brancaccio*[2], *Bruno Basile*[3], *Max J. Ammann*[1]

[1]*Antenna and High Frequency Research Centre, Dublin Institute of Technology, Kevin Street, Dublin 8, Ireland*
[2]*Dipartimento di Ingegneria Industriale e dell'Informazione, Seconda Università di Napoli, Via Roma 29, 81031 Aversa (CE), Italy*
[3] *B&B Sas, Strada Fienile 1, Napoli 80013, Casalnuovo di Napoli (NA), Italy*
✉ *E-mail: giuseppe.ruvio@dit.ie*

Published in Healthcare Technology Letters; Received on 11th January 2016; Revised on 21st May 2016; Accepted on 31st May 2016

This Letter introduces a feasibility study of a scanning system for applications in biomedical bone imaging operating in the microwave range 0.5–4 GHz. Mechanical uncertainties and data acquisition time are minimised by using a fully automated scanner that controls two antipodal Vivaldi antennas. Accurate antenna positioning and synchronisation with data acquisition enables a rigorous proof-of-concept for the microwave imaging procedure of a multi-layer phantom including skin, fat, muscle and bone tissues. The presence of a suitable coupling medium enables antenna miniaturisation and mitigates the impedance mismatch between antennas and phantom. The three-dimensional image of tibia and fibula is successfully reconstructed by scanning the multi-layer phantom due to the distinctive dielectric contrast between target and surrounding tissues. These results show the viability of a microwave bone imaging technology which is low cost, portable, non-ionising, and does not require specially trained personnel. In fact, as no a-priori characterisation of the antenna is required, the image formation procedure is very conveniently simplified.

1. Introduction: Microwave imaging has recently emerged as one of the most promising non-invasive imaging modalities of the last two decades. Its low cost, non-ionising characteristics justify the considerable interest of the scientific community. Although breast cancer imaging has been the most widely explored applications [1, 2], other biomedical diagnostic areas are also proposed [3, 4]. The operating principle is based on the dielectric contrast between the targeted and surrounding tissues. The imaging formation procedure involves illuminating the tissue with an electromagnetic radiation and analysing the reflected/scattered (and sometimes transmitted) signals from dielectric boundaries within the tissue. Several signal processing mechanisms to extract an image have been proposed. These algorithms can be divided into two broad categories: those that seek to identify the presence and location of significant dielectric scatterers in the tissue (termed as Radar approaches); and those whose aim is to reconstruct the entire dielectric profile of the tissue under examination (termed as tomographic approaches).

Ultra-wideband (UWB) antennas have been proven suitable for microwave medical imaging under Radar approaches due to their large operating bandwidth combined with stable radiation/coupling properties and compact designs [5, 6]. The antenna performance strongly affects the image formation procedure. Limited field penetration or non-uniform frequency-dependent near-field distribution can generate artefacts and degrade or destroy the imaging process. In order to fully assess the near-field microwave detection system performance, the antenna presence must be taken into account.

In [4, 7] microwave tomography was successfully introduced to image the heel in in-vivo measurements. The technique was proposed as non-invasive screening modality of osteoporosis bone cortex degradation. In this Letter, we present a microwave radar technique to image bone profiles in a more complex multi-tissue phantom that mimics a large leg. The system is capable of detecting the dielectric boundaries of two bones with different cross-sections that are embedded within a non-uniform multi-layer structure of skin, adipose and muscle tissues. An UWB signal is transmitted and received in the frequency bandwidth 0.5–4 GHz by two Vivaldi antennas in a radar monostatic fashion. The signal travels across different impedance conditions due to the heterogeneous scenario due to non-uniform multi-layer structure of skin, adipose, muscle and bone tissues. However, it also penetrates a highly attenuating muscle tissue that accounts for about 50% of the entire investigated volume. A fast localisation of the dielectric boundaries permits imaging of the bones profile.

This work shows the viability of microwave bone radar imaging technology which is low cost, portable, non-ionising and does not require specially trained personnel. In fact, microwave technology allows using compact and moderately expensive devices compared to other conventional imaging technologies. Images are reconstructed by using non-coherent migration, which is a particular version of beamforming [8, 9]. In particular, using non-coherent migration to reconstruct bone profiles from measured reflection coefficients makes unnecessary any pre-scan antenna characterization. This feature both speeds up the scanning time and ease usability.

After a brief description of its functional parts, results are shown in the following scenarios:

- A metal scatterer in homogeneous background totally filled with adipose tissue for delocalisation assessment.
- Bones inserted in a multi-layer structure including skin, fat and muscle.

2. Three-dimensional (3D) microwave scanner and phantom: The 3D scanner proposed here extends the investigation carried out in [9] for breast cancer detection in a more controlled environment and on a diverse target (Fig. 1). The prototype is made of the following parts:

- Two printed antipodal Vivaldi antennas that can be manoeuvred to adjust their height and distance from the phantom.
- A turntable that rotates the phantom with ±1° accuracy.
- A tank that contains the measuring setup immersed in a coupling medium with permittivity of 12.
- A vector network analyser to measure the S-parameters at the antennas' terminals.
- An acquisition unit to synchronise the antenna/phantom positioning with the data acquisition.
- A data processing unit to generate reconstructed images from the measured datasets.

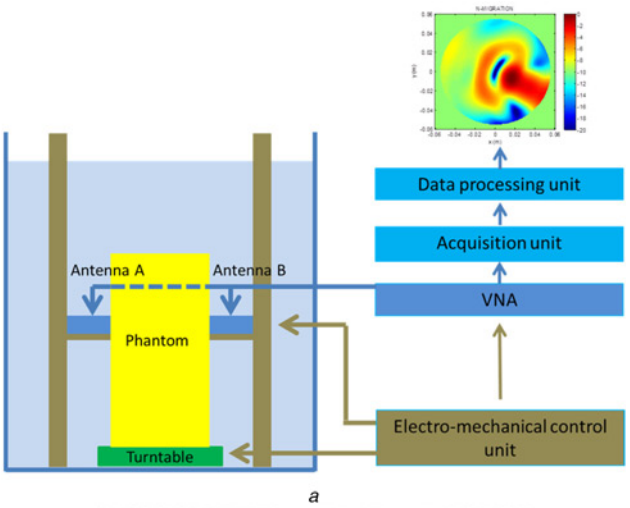

a

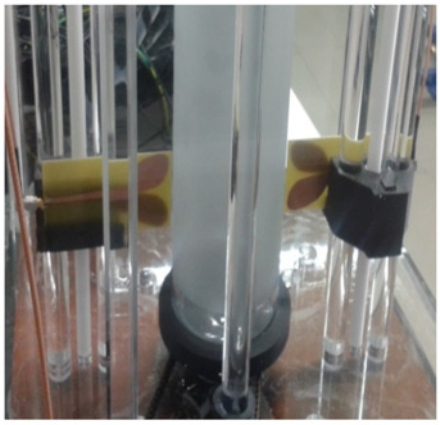

b

Fig. 1 *3D microwave scanner and phantom*
a Schematics of the scanning procedure with two antennas positioned on opposite sides of the phantom to half the scanning time
b Detail of the scanner

The geometry of the antenna is shown in Fig. 2 and consists of a printed element on 1.6-mm thick FR4 substrate. The dimensions and the taper of the two metallised parts were optimised to combine compactness with satisfactory field penetration inside the phantom. Each prototyped antenna was sprayed with 3M™ Novec™ coating to prevent electro-mechanical change of the dielectric when immersed in the coupling medium.

The system records S_{11} and S_{22} sampled across 801 equally spaced points in the frequency range 0.5–4 GHz, where satisfactory impedance matching is achieved (better than −8 dB). In this configuration, instead of having one single antenna scanning the phantom across 360° as in [9], two antennas are positioned on opposite sides of the phantom to half the scanning time. Hence, each antenna scans the phantom across complementary 180° angular sectors.

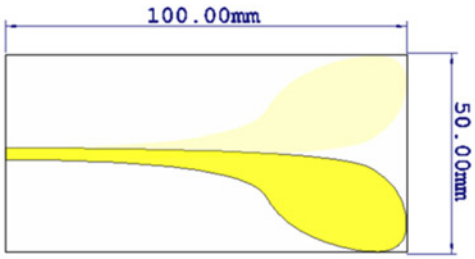

Fig. 2 *Geometry of the printed antipodal Vivaldi antenna*

The coupling medium used a mixture of 50% kerosene–50% safflower oil solution and de-ionised water in the proportion of 80 and 20%, respectively [10].

A realistic phantom that mimics a cow's leg was prepared by using a bovine tibia and fibula bone section with muscle tissue attached and embedded in pork fat and turkey skin for convenience (Fig. 3). By assembling the phantom, more control on the ratio between adipose and non-adipose tissue volumes can be achieved. This phantom was manufactured with the *bone* + *muscle* accounting for more than 80% of the entire volume in order to challenge the imaging procedure with high percentage of electromagnetically dense tissue in the scanned volume. The dielectric properties of the corresponding human tissues in the phantom are listed in Table 1 at the centre frequency of 2.75 GHz [10–12]. The phantom has an overall approximate diameter of 100 mm and a length of 250 mm with the bone-section of diameter 28 mm. Three slices in the central region spaced 10 mm apart were considered for screening with 36 scans per slice (18 per antenna).

The dielectric contrast between the target (i.e. bone) and surrounding tissues is about 4.6 which is significantly greater than that observed in microwave breast cancer imaging [10]. However, this scenario presents different challenges as the target bone tissue is embedded in a thick and electromagnetically denser layer of muscle tissue, hence results in a weaker signal reaching the target tissue.

3. Imaging procedure: The observation domain Γ is a set of circular lines each located at different heights, z_h. For a fixed height, the field scattered by the phantom is collected by a T_X/R_X antenna over N scanning positions ($\underline{r}_{01}$, $\underline{r}_{02}$, …, $\underline{r}_{0N}$) taken

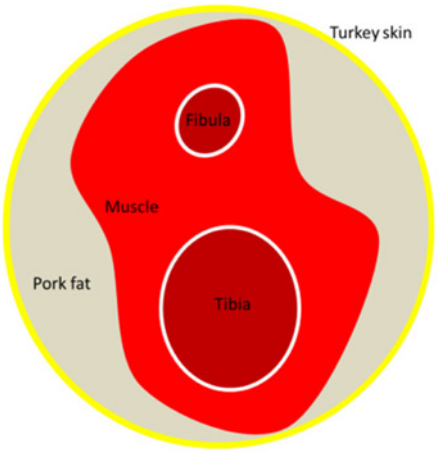

a

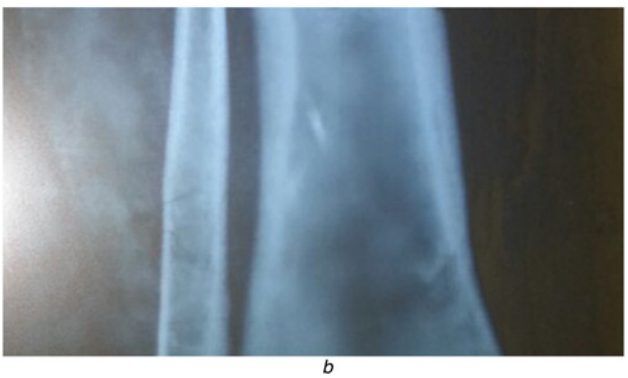

b

Fig. 3 *Realistic phantom that mimics a cow's leg was prepared by using a bovine tibia and fibula bone section*
a Phantom's cross-section
b Sagittal *X*-ray scan of the phantom

Table 1 Dielectric properties of corresponding human tissues in phantom at 2.75 GHz

	Conductivity, S/m	Relative permittivity
bone cortical	0.45429	11.207
marrow	0.10877	5.2644
muscle	1.9515	52.363
fat	0.11809	5.2492
skin	1.7802	42.442

uniformly around it at N_f frequency bins. The data of a complete scan can be arranged accordingly in the $N \times N_f$ scattering matrix $\underline{\underline{S}} = \left[\underline{S}_1, \ldots, \underline{S}_{n_f}, \ldots, \underline{S}_{N_f}\right]$ where $\underline{S}_{n_f}$ is the column vector of data collected over the observation positions at n_fth frequency. These data include the information signal, but also strong clutter components generated from the antenna's internal reflection, skin and other non-targeted tissues. As the clutter tends to mask the bone-interface signal, it has to be reduced before the image construction procedure. Different clutter rejection methods exist in the literature such as the differential approach, the subspace projection method and the entropy-based time windowing algorithm [13]. However, considering the cylindrical layout of the adopted phantom for this proof-of-concept, the *average trace subtraction* strategy is implemented. In particular, in frequency domain one obtains

$$\underline{\underline{S}}_{\mathrm{AV}} = \underline{\underline{S}} - \check{\underline{\underline{S}}} \tag{1}$$

where the subscript AV indicates that the average trace subtraction algorithm is used. Each column of the matrix $\check{\underline{\underline{S}}} = \left[\check{\underline{S}}_1, \ldots, \check{\underline{S}}_{n_f}, \ldots, \check{\underline{S}}_{N_f}\right]$ has values all equal to the average over the sensors' positions (fixed the frequency).

To test the detection system, the non-coherent migration is adopted according to the expression in the following equation

$$\phi_{N-M}(\underline{r}_k, z_h) = \sum_{i=1}^{N_f} \tag{2}$$

where $\underline{A}^k(f_i)$ is the steering vector calculated at the trial position $\underline{r}_k$ within the spatial domain D. The positions of the target are identified where the pseudo-spectrum $\phi_{N-M}(.)$ peaks, with $M_I[.]$ being migration operator [9]. Note that by employing non-coherent migration no information about the antenna is needed. In fact, as shown in [9] this algorithm actually represents a no-windowing beamforming image method. Therefore, as the time window is not considered, the travel time within the antenna is not required.

The data collected for each measurement position on the observation circle is used to generate a reconstruction of the corresponding 2D slice (i.e., in the x–y-plane). This operation is then repeated for each of the three slices considered. More in detail, both the de-clutter procedure and the calculation of the pseudo-spectrum $\phi_{N-M}(.)$ are repeated for each slice.

Hence, the final 3D reconstruction is obtained by performing a collection of 2D single pseudo-spectra at different heights. Once the 2D slice reconstructions are obtained, the 3D image of the target is obtained by superimposing the 2D reconstructions

$$I(\underline{r}_k) = \begin{pmatrix} \phi_{N-M}(\underline{r}_k, z_1) \\ \cdots \\ \phi_{N-M}(\underline{r}_k, z_H) \end{pmatrix} \tag{3}$$

where $z_h \in (z_1, \ldots, z_H)$ are the different heights at which the slices are taken. Finally, the actual 3D reconstruction is obtained by interpolating in the z-direction.

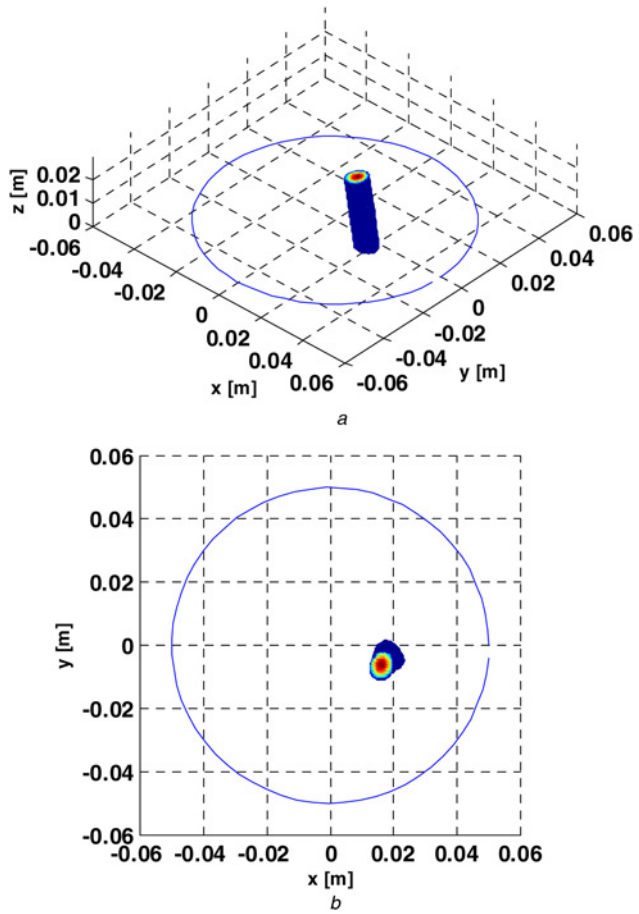

Fig. 4 *Target located at (x = 20 mm; y = −5 mm) is imaged*
a 3D reconstruction of the investigation scene totally filled with adipose tissue and an 8-mm thick cylindrical metal bar used as target
b Overhead view of 3D reconstruction

4. Results: The scanner was assessed for a very simple homogeneous scenario with the investigation scene totally filled with the coupling medium and an 8 mm thick cylindrical metal bar used as target. This test was performed in order to estimate the delocalisation error due to the mismatch of the equivalent permittivity used by the algorithm to generate the image from the actual permittivity of the coupling medium. Thirty-six equally spaced measurements were taken across three sections spaced 10 mm from each other.

In the top panel of Fig. 4, the target located at ($x = 20$ mm; $y = -5$ mm) is imaged. Although the object appears slightly oblique, the 3D reconstruction is successfully performed. In each of the three 2D reconstructions (omitted here for brevity) the target is detected with a consistent spatial displacement (SD) of 2.78, 2.85 and 4.23 mm, respectively. The SD measures the error in the target localisation and accounts for the difference between the target centre position as a peak value in the reconstruction and as actual centre position in the scanned phantom [14]. This is due to the mismatch between the adopted equivalent phantom permittivity in the reference Green's function and the actual unknown permittivity mapping of the detection scene. The bottom panel of Fig. 4 highlights once again the effect of the mismatch described above.

The phantom 3D image is shown in Fig. 5 when scanned across three sections spaced 10 mm apart. The presence of both tibia and

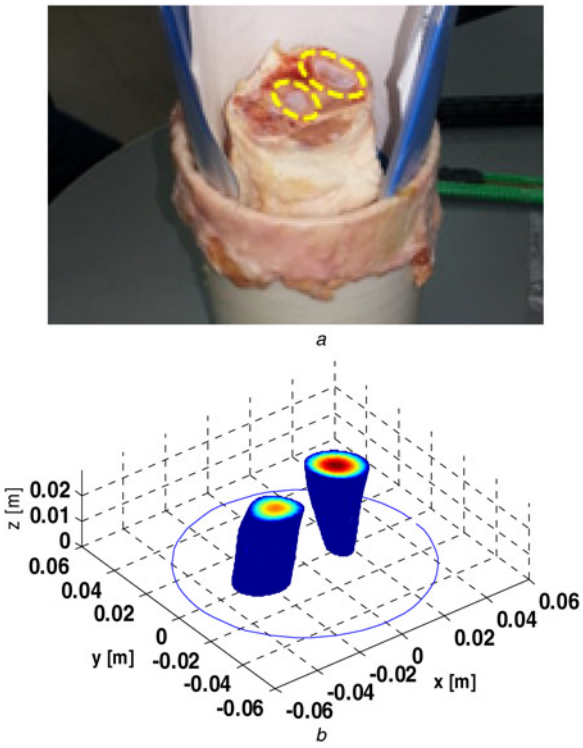

Fig. 5 *Phantom 3D image*
a Preparation of the realistic phantom (tibia and fibula are marked in yellow circle)
b 3D image reconstruction of the tibia and fibula in the phantom

fibula is correctly detected and their 3D profile is reconstructed. Although the different cross-sections of the bones are not distinguished by the imaging algorithm, the targets are localised in the scanned area with good accuracy.

5. Conclusions: The microwave scanning system presented here shows promising results for bone imaging in a multi-layer complex limb-mimicking phantom. Without a priori antenna characterisation, the image formation procedure based on non-coherent migration successfully reconstructs the 3D profile of both bones in the phantom. This feature greatly simplifies the scanner's operability.

Although the scenario under investigation presents several degrees of difficulty such as its multi-layer structure and the presence of more than one target (i.e. tibia and fibula) with different cross-sections, the scanner is able to discriminate the bone-muscle interface and reconstruct its 3D profile. Future work will explore the integration of a multi-element antenna array to enable multi-view radar configurations. On a more engineering side, a more compact version of the prototyped scanner will be designed to deliver a portable bone scanning device that can be used in site of accidents. This application can be advantageous for faster assessment of nonobvious Greenstick fractures.

6. Funding and declaration of interests: This work was supported by Italian Ministry of University and Research through the FIRB initiative under the project MICENEA (RBFR12A7CD) and the COST Actions TD1301 MiMed and BM1309 EMF-MED. Dr. Basile has a patent 102016000000228 pending.

7 References

[1] Nikolova N.K.: 'Microwave imaging for breast cancer', *IEEE Microw. Mag.*, 2011, **12**, (7), pp. 78–94
[2] Fear E.C., Meaney P.M., Stuchly M.A.: 'Microwaves for breast cancer detection?', *IEEE Potentials*, 2003, **22**, (1), pp. 12–18
[3] Fhager A., Persson M.: 'A microwave measurement system for stroke detection'. Seventh Loughborough Antennas and Propagation Conf., LAPC 2011, Loughborough, 14–15 November 2011
[4] Tian Z., Meaney P.M., Pallone M.J., *ET AL.*: 'Microwave tomographic imaging for osteoporosis screening: a pilot clinical study'. Conf. Proc. IEEE Engineering in Medical and Biology Society, 2010, pp. 1218–1221
[5] Jafari H.M., Deen M.J., Hranilovic S., *ET AL.*: 'A study of ultrawideband antennas for near-field imaging', *IEEE Trans. Antennas Propag.*, 2007, **55**, (4), pp. 1184–1188
[6] Flores-Tapia D., Pistorius S.: 'Real time breast microwave radar image reconstruction using circular holography: a study of experimental feasibility', *Med. Phys.*, 2011, **38**, pp. 5420–5431
[7] Meaney P.M., Goodwin D., Golnabi A., *ET AL.*: '3D Microwave Bone Imaging'. Proc. Sixth European Conf. on Antennas and Propagation (EUCAP), 2011, pp. 1170–1171
[8] Solimene R., Ruvio G., Dell'Aversano A., *ET AL.*: 'Detecting point-like sources of unknown frequency spectra', *Prog. Electromagn. Res.*, 2013, **B**, (50), pp. 347–364
[9] Ruvio G., Solimene R., Cuccaro A., *ET AL.*: 'Breast cancer detection using interferometric MUSIC: experimental and numerical assessment', *Med. Phys.*, 2014, **41**, (10), pp. 103101/1–103101/11
[10] Gabriel C.: 'Compilation of the dielectric properties of body tissues at RF and microwave frequencies'. Report N.AL/OE-TR- 1996-0037, Occupational and Environmental Health Directorate, Radiofrequency Radiation Division, Brooks Air Force Base, Texas (USA), June 1996
[11] Gabriel C., Gabriel S., Corthout E.: 'The dielectric properties of biological tissues: I. Literature survey', *Phys. Med. Biol.*, 1996, **41**, pp. 2231–2249
[12] Gabriel S., Lau R.W., Gabriel C.: 'The dielectric properties of biological tissues: II. Measurements in the frequency range 10 Hz to 20 GHz', *Phys. Med. Biol.*, **1996**, 41, 2251–2269
[13] Solimene R., Cuccaro A.: 'Front wall clutter rejection methods in TWI', *IEEE Geosci. Remote Sens. Lett.*, 2013, **11**, pp. 1158–1162
[14] Coincecao R.C., O'Halloran M., Glavin M., *ET AL.*: 'Comparison of planar and circular antenna configurations for breast cancer detection using microwave imaging', *Progr. Electromagn. Res.*, 2009, **99**, pp. 1–20